Journal of Alloys and Compounds 813 (2020) 152232

Contents lists available at ScienceDirect

Journal of Alloys and Compounds

journal homepage: http://www.elsevier.com/locate/jalcom

Unravelling atomically resolved structure of a high-*k* dielectric oxide-semiconductor interface: Exit wave reconstruction and ab-initio calculation insights

Mahabul Islam [a, b], Piu Rajak [a], Satyesh Kumar Yadav [a], Somnath Chanda Roy [b], Somnath Bhattacharyya [a, *]

[a] Department of Metallurgical and Materials Engineering, Indian Institute of Technology Madras, Chennai, 600036, India
[b] Department of Physics, Indian Institute of Technology Madras, Chennai, 600036, India

ARTICLE INFO

Article history:
Received 20 August 2019
Received in revised form
6 September 2019
Accepted 9 September 2019
Available online 10 September 2019

Keywords:
Heterostructure
Interface
Transmission electron
Microscopy
Exit wave reconstruction
Argand plot
DFT

ABSTRACT

Heterostructure interfaces play a major role in defining the performance of thin-film devices. High-*k* dielectric oxide-semiconductor heterostructures are being extensively investigated as promising candidates for future integrated circuits, thus it becomes important to precisely probe the interfaces at the atomic scale for technological advancements. In this work, a high-*k* dielectric oxide (Gd_2O_3)-semiconductor (Ge) interface was characterized at the atomic scale using complex-valued exit wave reconstructed from a set of focal series high-resolution transmission electron microscopy (HRTEM) images acquired without objective lens spherical aberration correction. The complexity of this characterization lies in removing image artefacts produced by amorphous layer deposited on the imaged region during ion milling which was successfully solved using an algorithm to remove amorphous background developed recently. The final result reveals that the interface of the present study is atomically sharp and flat. The thickness of the imaged region along viewing direction was estimated from channelling map. Comparing reconstructed amplitude of experimental data with that of simulated one generated using Density Functional Theory (DFT) optimized interface structure, it was found that the Gd_2O_3 layers were terminated at the Gd atoms in the interface.

1. Introduction

Solid-solid interfaces comprise of local, non-periodic structural characteristics, defects and disorder that are important to understand from an application perspective as the interface controls the overall properties of a device [1]. Catalysis [2,3], charge and spin transport [4], polymerization [5] are some of the important and critical processes that take place at different kinds of interfaces. Further, interesting magnetic effects may arise due to symmetry breaking at interfaces [4,6]. To integrate new materials into devices, the structure, microstructure and properties of interfaces with different materials must be thoroughly established. Consequently, interfaces play a crucial role in developing new materials to meet today's challenges [7]. Complementary metal-oxide-semiconductor (CMOS) [8] is a rapidly growing technology for designing integrated circuits. It requires substituting the traditional gate oxide (e.g. SiO_2), with high-*k* dielectrics which can maintain the same capacitance with much lower leakage current [9,10]. The most favourable materials for the next generation CMOS technology are the high-*k* oxides with high mobility channel materials (e.g. Ge, III–V semiconductor) on Si substrates [10]. In some cases, germanium (Ge) is preferred as channel material in CMOS devices over Si for its higher electron mobility [11]. Encapsulated solid phase epitaxy is an effective approach to grow an epitaxial Ge layer within epitaxial rare earth oxide Gd_2O_3 [12] which is proposed to be a potential candidate for resonant tunnelling device at room temperature. But the diffuseness of high-*k* dielectric oxide-semiconductor interface may degrade device performance severely. Hence, it becomes necessary to probe these interfaces precisely at atomic scale to predict the device performance a priori.

Experimentally, the local atomic structure of the interface can be probed by different high-resolution transmission electron microscopy (HRTEM) techniques [13]. The challenge to study an interface

* Corresponding author.
E-mail address: somnathb@iitm.ac.in (S. Bhattacharyya).

https://doi.org/10.1016/j.jallcom.2019.152232
0925-8388/

using any HRTEM techniques lies in successfully removing image artefacts produced by amorphous layer deposited on the imaged region during ion milling. These artefacts alter image features and this effect increases with increasing amorphous layer thickness [14]. The source of these amorphous layers could either be the leftover of epoxy glue used in conventional cross-sectional TEM specimen preparation and/or elements from the material itself knocked out during ion beam milling.

In this study, Ge (111)/Gd_2O_3 (111) interface of an encapsulated Gd_2O_3-Ge-Gd_2O_3 heterostructure grown using encapsulated solid-phase epitaxy [12] was studied at atomic scale using the amplitude of the complex-valued exit wave reconstructed using a set of focal series HRTEM images acquired without objective lens spherical aberration correction. By comparing reconstructed amplitude of experimental data with that of optimized interface structure using Density Functional Theory (DFT), the possible atomic termination in Gd_2O_3 side was assessed.

2. Methods

2.1. TEM sample preparation and imaging

Growth of Gd_2O_3-Ge-Gd_2O_3 heterostructure was carried out on *p*-Si (111) substrate using a molecular beam epitaxy (MBE) system [12] and subsequent cross-sectional sample preparation for TEM imaging [15] was reported earlier. During sample preparation, two small pieces from the heterostructure thin film were cut perpendicular to the growth direction and were sandwiched using G1 epoxy (Gatan Inc.). This sandwiched structure was placed within a Titanium 3 slots grid (Technoorg Linda Co. Ltd.) and was thinned down from both sides to electron transparency. HRTEM imaging was done using FEI-TITAN TEM operated at 300 kV equipped with field emission gun (FEG) source and GIF "Tridem" energy filter. Gd_2O_3 (111)/Ge (111) interface was made parallel to the electron beam by tilting the interface to [1$\bar{1}$0]. Digital Micrograph software (Gatan Inc., USA) was used to acquire a series of HRTEM images on a 2K × 2K CCD camera at different defocuses. In the present work, a stack of 15 images with defocus value ranging from −35 nm to +35 nm with a step of 5 nm was used to reconstruct the exit face wave function using FRWR [16] software.

2.2. DFT simulations

The DFT method has proven to be one of the most accurate methods for the computation of the electronic structure of solids [17–25]. DFT calculations as implemented in the Vienna Ab-Initio Simulation Package (VASP) [26] code were performed to obtain the optimized atomic Ge/Gd_2O_3 heterostructure that was used further for simulating HRTEM images of Ge (111)/Gd_2O_3 (111) interface. The pseudopotentials based on the projector-augmented-wave method [27] explicitly include the following valence electronic configurations for different elemental species: O: $2s^2 2p^4$, Ge: $4s^2\ 4p^2$, and Gd: $4f^7\ 5s^2\ 5p^6\ 5d^1 6s^2$. The exchange-correlation energy function was treated at the generalized gradient approximation (GGA) level employing the Perdew–Burke–Ernzerhof (PBE) functional [28]. Optimized lattice parameters for Ge belonging to Fd$\bar{3}$m space group and Gd_2O_3 belonging to Ia$\bar{3}$ space-group were 5.78 Å and 9.36 Å respectively. These values are in good agreement with previously reported results [29,30] at a similar level of theory. The Kohn-Sham wave functions were expanded in plane-wave basis-sets [31] up to an energy cutoff of 520 eV with energy convergence criterion for total energy within 0.01 meV for both unit cells and forces required to be less than 0.02 eV $Å^{-1}$. Monkhorst type K-meshes of 4 × 4 × 4 and 8 × 8 × 8 types were used to sample the first Brillouin zone of Ge and Gd_2O_3, respectively. To correct for the strong on-site f–f interactions, Hubbard U corrections were done as suggested in Refs. [32,33] with Hubbard parameters U = 8 eV, J = 0 eV was considered for Gd 4f orbitals for GGA + U [34] calculation.

To gain insights into the nature of the interface, Ge (111)/Gd_2O_3 (111) system was systematically studied using DFT calculations according to the experimental conditions. To identify the possible atomic structures of the interface, both Gd and O-terminated slab structures for Gd_2O_3 along [111] direction were considered. For building the vacuum slab model of Ge (111)/Gd_2O_3 (111), 4 atomic layers of O-terminated Gd_2O_3 (111) slab and 4 atomic layers of Ge (111) slab were stacked along [111] direction as shown in Fig. S1(a) (supplementary section) to create oxygen terminated interface; similarly, 4 atomic layers of Gd-terminated Gd_2O_3 (111) slab and 4 atomic layers of Ge (111) slab were also stacked along [111] direction as shown in S1(b) (supplementary section) to create Gd-terminated interface. There are several possible in-plane configurations of Ge slab with respect to Gd_2O_3 slab. Atomic configuration of Ge and O atoms at the interface plane for Gd and O terminated slabs are shown Fig. S1(c) and Fig. S1(d) in the supplementary section, respectively. The choice of this in-plane configuration is justified as oxygen atoms lie directly below the Ge atoms. The top layer of Ge and the bottom layer of Gd were allowed to relax only along the c direction [111], all other atoms were allowed to relax in all directions. 1 × 1 × 1 Monkhorst-Pack k points grid was used to relax atoms while keeping the shape and size of supercell fixed.

2.3. TEM image simulation of optimized DFT model structure

To compare with experimental data, HRTEM images were simulated using multislice algorithm with frozen phonon approximation. QSTEM [35,36] software package has been used to simulate HRTEM images at different defocus. The simulation parameters were set at similar experimental conditions. All TEM images were simulated along [1$\bar{1}$0] with thermal diffuse scattering (TDS) [37]. Two Ge/Gd_2O_3 interface models one with Gd and another with O-terminated slab obtained from DFT calculation were used for HRTEM image simulation. To obtain a comparable match with experimental images, Poisson noise was applied to the simulated TEM images. A set of 15 images with defocus ranging from −35 nm to 35 nm with a defocus step of 5 nm have been simulated and were used to reconstruct the complex-valued exit wave using the FRWR [16] software.

3. Results and discussions

Fig. 1 shows an HRTEM image from a set of focal series images of interface along [1$\bar{1}$0] zone axis where left hand side of the interface

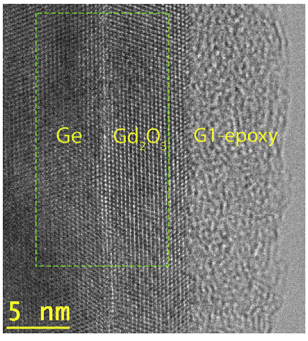

Fig. 1. An HRTEM image from a set of focal series images of the interface along [1$\bar{1}$0] zone axis.

is Ge (111) and right hand side is Gd_2O_3 (111). Between the Gd_2O_3 and vacuum, there is a region with leftover amorphous epoxy that was used for preparing a cross-sectional TEM specimen. All regions are marked in the image itself. The region around the interface marked with green box was considered to reconstruct the complex-valued exit wave. Fig. 2a and b represent the amplitude and phase of the reconstructed complex-valued exit wave respectively. Reconstructed complex-valued exit wave has less image distortions produced by the projector lens and delocalization due to coherent aberrations of the objective lens than experimental HRTEM images. The spatial resolution of the reconstructed data is ~1 Å as calculated from the power spectrum of the reconstructed phase shown in Fig. S2 in the supplementary section. Fig. 2a and b do not allow us to unambiguously comment on the sharpness and position of the interface as they reveal random contrast variations on very short length scale in both sides of the interface. These unusual variations can be caused due to random specimen thickness variation along the electron beam direction. Thickness variation produced by ion beam milling during TEM sample preparation can safely be ruled out because both Ge and Gd_2O_3 sides are single crystalline and variations are observed in much shorter length scale than usually produced by ion beam milling. Another reason of this thickness variation could be due to the accumulation of amorphous materials of varying thicknesses within imaged region similar like Fig.5 of reference [14]. Power spectrum presented in Fig. S3b from Ge side of Fig. 2b reveals sufficient background which confirms the presence of amorphous within imaged region. Fig. 1 shows 6–8 nm long leftover of amorphous epoxy glue adjacent to the edge that was used to make cross-sectional sandwich sample during TEM sample preparation. Therefore, the accumulated amorphous materials on imaged region are expected to be the epoxy glue that might have spread on imaged region during ion beam milling. A portion of Ge side from Fig. 2b and corresponding principle strain components within the region calculated using Geometrical Phase analysis (GPA) method [38] are presented in Fig. S3 which reveals random strain variations within the Ge region. Similar like previous report [14], in the present work the random contrast as well as strain variations within the imaged region are nothing but artefacts induced by the amorphous epoxy glue. To remove these artefacts, reconstructed amplitude and phase were processed with an algorithm reported earlier [39]. Amplitude and phase after removing amorphous epoxy glue induced artefacts were presented in Fig. 2c and d respectively which helps to infer qualitatively that the interface is atomically sharp and flat as indicated by the dotted lines in both the figures. It can be stated here that in order to comment on the sharpness and/or structure of an interface in close proximity to amorphous epoxy in cross-sectional TEM samples, special care must be taken to remove the epoxy induced artefacts.

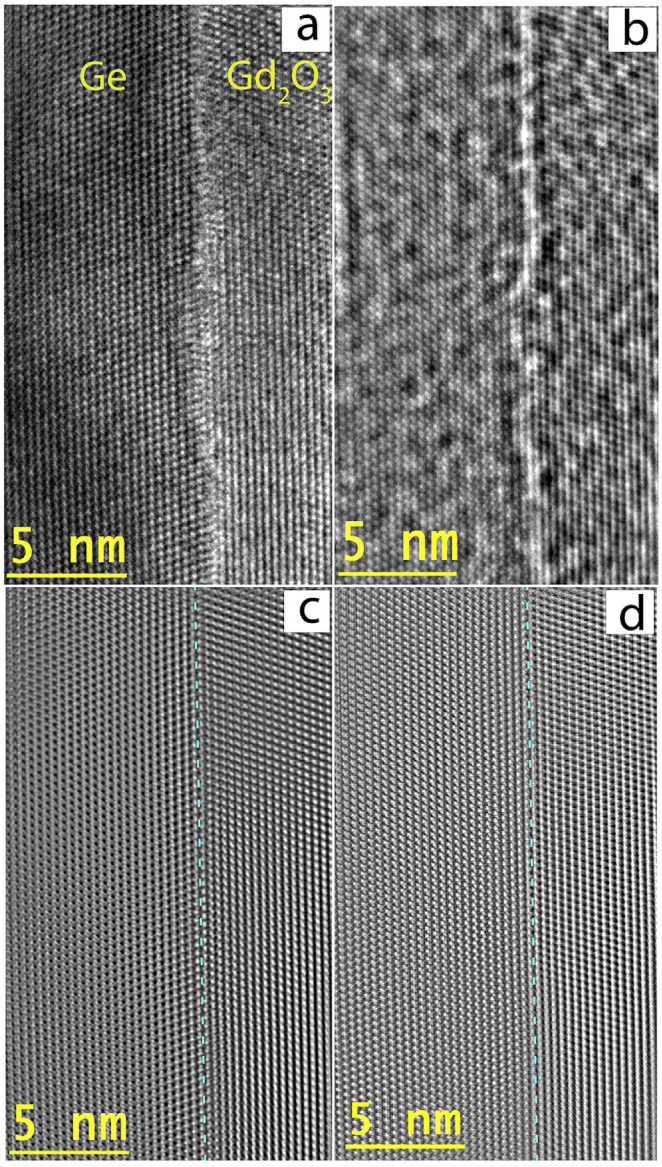

Fig. 2. (a) Amplitude and (b) phase of the complex-valued exit wave reconstructed using a set of focal series images from the region encompassed with a green box in Fig. 1. (c) and (d) represent the amplitude and phase of the reconstructed complex-valued exit wave after removing the amorphous epoxy induced artefacts, respectively where the interface positions are indicated with cyan dashed lines. (For interpretation of the references to colour in this figure legend, the reader is referred to the Web version of this article.)

To determine the position of the interface more accurately, magnified version of three regions of the artefacts removed amplitudes (Fig. 2c) are presented in Fig. 3a–c. All three regions shown here have an almost same thickness along the viewing direction across the interface (relative thickness map in Fig. S3 of the supplementary section). To determine the position of the interface accurately, intensity profiles from interface towards left sides and towards right sides are presented in Fig. 3d–f and Fig. 3g–i respectively. Blue boxes in Fig. 3a–c indicated the regions from where intensity profiles were taken. It can be noted that for each imaged region in Fig. 3a–c, intensity profiles of left hand side of the interface has a lower value than that on the right-hand side. Using phase object approximation [40], it can be stated that the change in amplitude is mainly due to the change in inelastic scattering potential when thickness along the viewing direction remains the same. Since Gd ($Z = 64$) has a higher atomic number than Ge ($Z = 32$), it is expected that the left side region containing Ge should have a different value of amplitude than that of right side region containing Gd, which is evident from the comparison of intensity profiles of the left and right side for each region. Therefore, it can be inferred that the interface of the present study is atomically sharp.

To study the interfacial structure further, it is important to determine the thickness of the imaged region along the viewing direction. Initially, the thickness was determined using log ratio method [41]. Detailed determination is presented in the supplementary section which reveals that across the Ge (111)/Gd_2O_3 (111) interface the relative specimen thickness remains unchanged. Furthermore, specimen thickness was determined more precisely at the Ge side of the interface based on electron channelling theory [42–45]. A Ge [$1\bar{1}0$] wedge-shaped crystal varying from 1 to 14 atoms with a step size of 1 atom and width of 3 atoms was built and

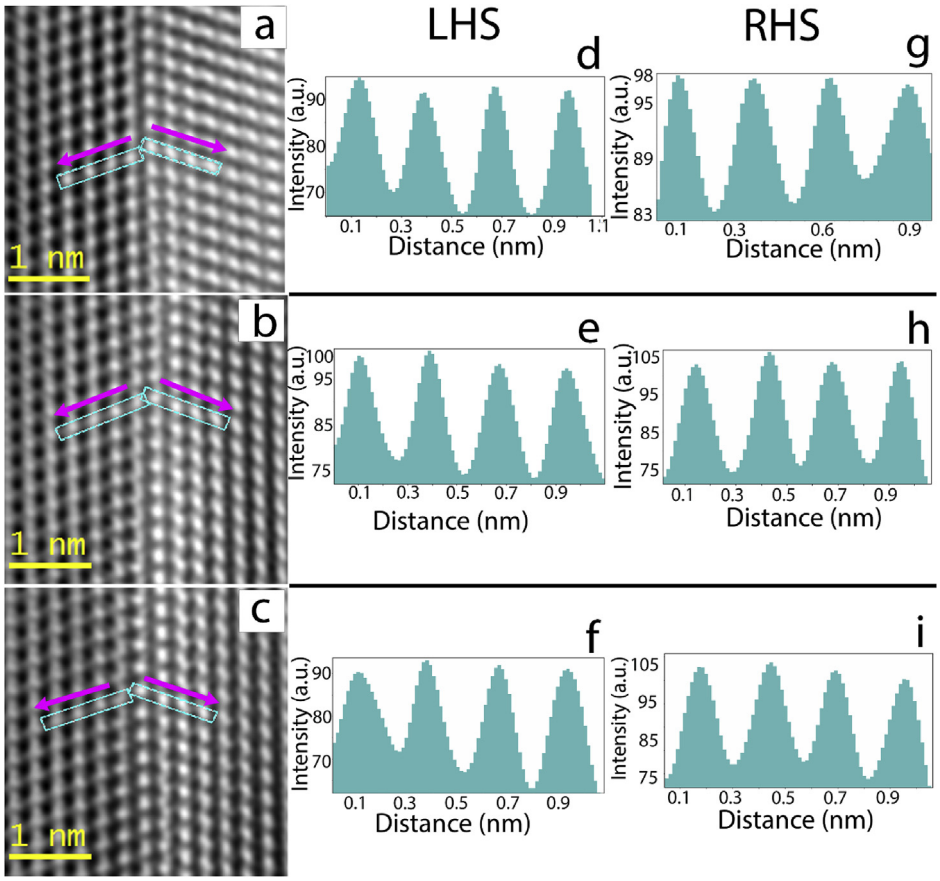

Fig. 3. Magnified versions of three regions from (a) top, (b) middle and (c) bottom portion of Fig. 2c. (d)–(f) are intensity profiles from interface towards left sides and (g)–(i) are towards right sides of the interface taken from the respective regions encompassed with green boxes. (For interpretation of the references to colour in this figure legend, the reader is referred to the Web version of this article.)

exit wave at 300 kV using same parameters as of experiment was calculated using multislice algorithm. Structural model, reconstructed amplitude and phase are presented in Figs. S4a–S4c of the supplementary section respectively. Argand plot of the exit wave (ψ) of wedge-shape Ge in [1$\bar{1}$0] with data points and fitted circle marked in blue is presented in Fig. 4a. This is the most effective way to visualize the exit wave where the complex value of each pixel follows a circular locus and the angular increment is proportional to the number of atoms in a column. The circle of the Argand diagram consists of 14 data points each corresponding to one extra Ge atom in the column. The discrete nature of Argand plot reveals, in general, that each atomic column contains different number of Ge atoms and the thickness increases atom by atom along the counter clockwise direction of the circle. Fig. 4b represents an angular distribution of the exit wave phase and phase change per Ge atom was calculated to be ~0.26 rad. The red circle with data points in Fig. 4a corresponds to the Argand plot of reconstructed exit wave of the Ge side of the experimental interface where a single bunch of data points located at a particular angle corresponds to a specific thickness. From data points marked in red the angular position (θ), w.r.t vacuum wave (green dot) was calculated to be ~3 rad which is equivalent to 12 Ge atoms along viewing direction. Thus the calculated thickness of the imaged region is ~2.5 nm.

The next objective was to determine the type of termination at the interface on Gd_2O_3 side. Using DFT optimized Gd and O-terminated interface models shown in Fig. 4c and e respectively, focal series of HRTEM images were simulated for 2.5 nm thicknesses along the viewing direction and complex-valued exit waves were reconstructed using these focal series. Reconstructed amplitudes of Gd and O truncated interfaces are shown in Fig. 4d and f respectively and corresponding reconstructed phases are in depicted in Figs. S5a and S5b of the supplementary section. Interface features of Fig. 4d closely matches with that of the reconstructed amplitude of the experimental interface shown in Fig. 3 than Fig. 4f. In Fig. 4f there exists a layer of ~0.7 nm where contrast is weaker than both Ge and Gd layers. This is because of atomic 'rearrangement' of Ge at the interface adjacent to oxygen atoms which are not evident from experimental micrographs. From this observation, it is concluded that the experimental interface truncates at Gd atoms in Gd_2O_3 side.

4. Conclusions

In the present work, a high-*k* dielectric oxide-semiconductor interface Ge (111)/Gd_2O_3 (111) was precisely characterized at the atomic scale. After removing the artefacts induced by amorphous layer deposited on top and/or bottom of the imaged region from the amplitude and phase of the reconstructed complex-valued exit wave, the interface is atomically sharp and flat. Specimen thickness along the electron beam of the imaged region was determined using Argand diagram based on electron channelling theory. Comparing reconstructed amplitude of experimental data with that of simulated one, the interface was found to be Gd-terminated in Gd_2O_3 side.

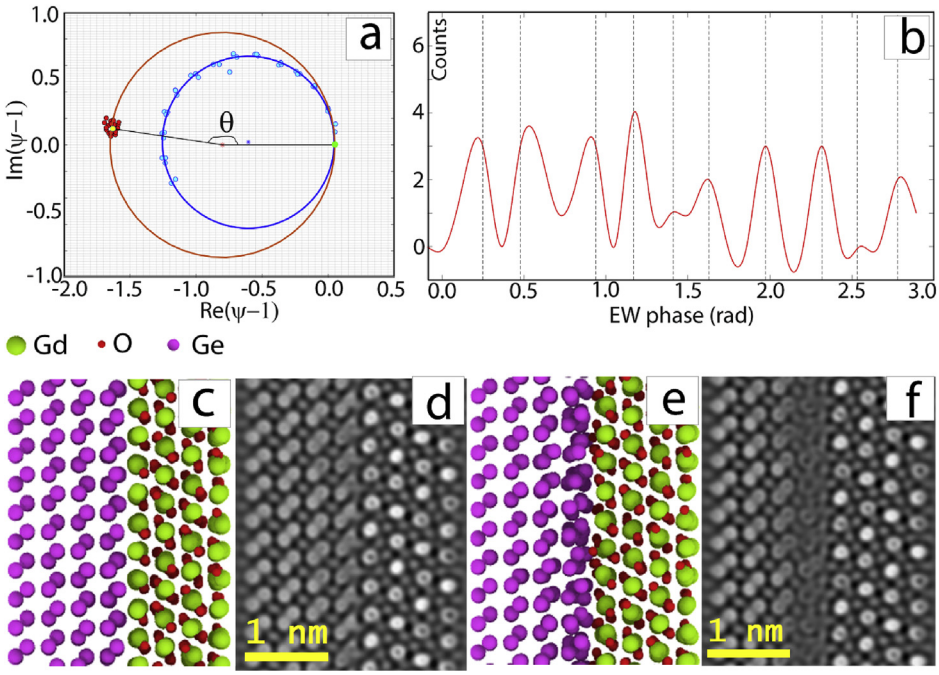

Fig. 4. (a) Argand plots using channelling theory. The blue circle with data points correspond to wedge-shaped Ge [1$\bar{1}$0] and a red circle with data points correspond to reconstructed exit wave of the Ge side of the experimental interface. The green dot at 3 O′ clock position corresponds to vacuum wave. (b) angular distribution of the exit wave phase of simulated wedge-shaped Ge [1$\bar{1}$0]. (c) and (e) DFT optimized Gd and O-terminated interface models respectively. (d) and (f) reconstructed amplitudes from the simulated focal series HRTEM images at thickness ~ 2.5 nm of interface structures shown in (c) and (e) respectively. (For interpretation of the references to colour in this figure legend, the reader is referred to the Web version of this article.)

Conflicts of interest

The authors declare no competing financial interest.

Acknowledgements

The financial assistance from the Science and Engineering Research Board (SERB), core research grant project no. EMR/F/2017/001510 is highly acknowledged. The High-Performance Computing Environment (HPCE) maintained by P. G. Senapathy Center for Computing Resource at the Indian Institute of Technology Madras (IITM) is acknowledged for computing facilities. M.I. acknowledges MHRD, India for financial support through HTRA (teaching assistantship).

Appendix A. Supplementary data

Supplementary data to this article can be found online at https://doi.org/10.1016/j.jallcom.2019.152232.

References

[1] K. Kobashi, R. Hayakawa, T. Chikyow, Y. Wakayama, Interface engineering for controlling device properties of organic antiambipolar transistors, ACS Appl. Mater. Interfaces 10 (2018) 2762–2767, https://doi.org/10.1021/acsami.7b14652.
[2] G. Li, K.A. Gray, The solid-solid interface: explaining the high and unique photocatalytic reactivity of TiO_2-based nanocomposite materials, Chem. Phys. 339 (2007) 173–187, https://doi.org/10.1016/j.chemphys.2007.05.023.
[3] Z. Xu, H. Wang, Y. Wen, W. Li, C. Sun, Y. He, Z. Shi, L. Pei, Y. Chen, S. Yan, Z. Zou, Balancing catalytic activity and interface energetics of electrocatalyst-coated photoanodes for photoelectrochemical water splitting, ACS Appl. Mater. Interfaces 10 (2018) 3624–3633, https://doi.org/10.1021/acsami.7b17348.
[4] F. Hellman, A. Hoffmann, T. Yaroslav, G.S.D. Beach, E.E. Fullerton, A.H. Macdonald, D.C. Ralph, Y. Tserkovnyak, G.S.D. Beach, E.E. Fullerton, C. Leighton, A.H. Macdonald, D.C. Ralph, D.A. Arena, H.A. Dürr, F. Peter, G. Julie, H.P. Joseph, T. Jungwirth, A. Kimel V, Interface-induced phenomena in magnetism, Rev. Mod. Phys. 89 (2017), 025006. https://doi.org/10.1103/RevModPhys.89.025006.
[5] M. Trchová, I. Šeděnková, J. Stejskal, In-situ polymerized polyaniline films 6. FTIR spectroscopic study of aniline polymerisation, Synth. Met. 154 (2005) 1–4, https://doi.org/10.1016/j.synthmet.2005.07.001.
[6] Z.Q. Qiu, S.D. Bader, Symmetry breaking at magnetic surfaces and interfaces, Surf. Sci. 438 (1999) 319–328, https://doi.org/10.1016/S0039-6028(99)00597-X.
[7] S. Borkar, I. Corporation, Design challenges of technology scaling, Ieee Micro (1999) 23–29.
[8] E. Fortunato, P. Barquinha, R. Martins, Oxide semiconductor thin-film transistors: a review of recent advances, Adv. Mater. 24 (2012) 2945–2986, https://doi.org/10.1002/adma.201103228.
[9] J. Robertson, R.M. Wallace, High-K materials and metal gates for CMOS applications, Mater. Sci. Eng. R Rep. 88 (2015) 1–41, https://doi.org/10.1016/j.mser.2014.11.001.
[10] A. Molle, S. Baldovino, S. Spiga, M. Fanciulli, High permittivity materials for oxide gate stack in Ge-based metal oxide semiconductor capacitors, Thin Solid Films 518 (2010) S96–S103, https://doi.org/10.1016/j.tsf.2009.10.065.
[11] D.L. Rode, Electron mobility in Ge, Si, and GaP, Phys. Status Solidi 53 (1972) 245–254, https://doi.org/10.1002/pssb.2220530126.
[12] A. Laha, E. Bugiel, M. Jestremski, R. Ranjith, A. Fissel, H.J. Osten, Encapsulated solid phase epitaxy of a Ge quantum well embedded in an epitaxial rare earth oxide, Nanotechnology 20 (2009) 475604, https://doi.org/10.1088/0957-4484/20/47/475604.
[13] J.C. Meyer, C. Kisielowski, R. Erni, M.D. Rossell, M.F. Crommie, A. Zettl, Direct imaging of lattice atoms and topological defects in graphene membranes - nano letters (ACS publications), Nano Lett. 8 (2008) 3582–3586. https://pubs.acs.org/doi/abs/10.1021/nl801386m.
[14] M. Settem, P. Rajak, M. Islam, S. Bhattacharyya, Influence of supporting amorphous carbon film thickness on measured strain variation within a nanoparticle, Nanoscale 9 (2017) 17054–17062, https://doi.org/10.1039/c7nr04334a.
[15] T. Das, S. Bhattacharyya, Structure and chemistry across interfaces at nano-scale of a ge quantum well embedded within rare earth oxide layers, Microsc. Microanal. 17 (2011) 759–765, https://doi.org/10.1017/S1431927611000559.
[16] C.T. Koch, A flux-preserving non-linear inline holography reconstruction algorithm for partially coherent electrons, Ultramicroscopy 108 (2008) 141–150, https://doi.org/10.1016/j.ultramic.2007.03.007.
[17] A.H. Reshak, Z.A. Alahmed, J. Bila, Phase transition in $BaThO_3$ from Pbnm to Ibmm turn the fundamental energy band gap from indirect to direct, J. Alloy. Comp. 771 (2019) 607–613, https://doi.org/10.1016/j.jallcom.2018.08.134.
[18] N.B. Stambouli, T. Ouahrani, M. Badawi, A.H. Reshak, S. Azizi, Untangling electronic, optical and bonding properties of hexagonal bismuth borate $SrBi_2B_2O_7$ crystal for ultraviolet opto-electronic applications: an ab initio

study, J. Alloy. Comp. 803 (2019) 1127–1135, https://doi.org/10.1016/j.jallcom.2019.06.346.
[19] A.H. Reshak, Y.M. Kogut, A.O. Fedorchuk, O.V. Zamuruyeva, G.L. Myronchuk, O.V. Parasyuk, H. Kamarudin, S. Auluck, K.J. Plucinski, J. Bila, Linear, non-linear optical susceptibilities and the hyperpolarizability of the mixed crystals $Ag_{0.5}Pb_{1.75}$ $Ge(S_{1-x}$ $Se_x)_4$: experiment and theory, Phys. Chem. Chem. Phys. 15 (2013) 18979–18986, https://doi.org/10.1039/c3cp53431f.
[20] A.H. Reshak, Ab initio study of TaON, an active photocatalyst under visible light irradiation, Phys. Chem. Chem. Phys. 16 (2014) 10558–10565, https://doi.org/10.1039/c4cp00285g.
[21] G.E. Davydyuk, O.Y. Khyzhun, A.H. Reshak, H. Kamarudin, G.L. Myronchuk, S.P. Danylchuk, A.O. Fedorchuk, L.V. Piskach, M.Y. Mozolyuk, O.V. Parasyuk, Photoelectrical properties and the electronic structure of Tl_{1-x} $In_{1-x}Sn_xSe_2$ (x = 0, 0.1, 0.2, 0.25) single crystalline alloys, Phys. Chem. Chem. Phys. 15 (2013) 6965–6972, https://doi.org/10.1039/c3cp50836f.
[22] A.H. Reshak, D. Stys, S. Auluck, I.V. Kityk, Dispersion of linear and nonlinear optical susceptibilities and the hyperpolarizability of 3-methyl-4-phenyl-5-(2-pyridyl)-1,2,4-triazole, Phys. Chem. Chem. Phys. 13 (2011) 2945–2952, https://doi.org/10.1039/c0cp01601b.
[23] A.H. Reshak, $Fe_2MnSi_xGe_{1-x}$ Influence thermoelectric properties of varying the germanium content, RSC Adv. 4 (2014) 39565–39571, https://doi.org/10.1039/c4ra02669a.
[24] A.H. Reshak, Thermoelectric properties for AA- and AB-stacking of a carbon nitride polymorph (C_3N_4), RSC Adv. 4 (2014) 63137–63142, https://doi.org/10.1039/c4ra13342k.
[25] A.H. Reshak, Spin-polarized second harmonic generation from the antiferromagnetic CaCoSO single crystal, Sci. Rep. 7 (2017) 1–8, https://doi.org/10.1038/srep46415.
[26] G. Kresse, J. Furthmuller, Efficient iterative schemes for ab initio total-energy calculations using a plane-wave basis set, Phys. Rev. B. 54 (1996) 11169–11186, https://doi.org/10.1103/PhysRevB.54.11169.
[27] G. Kresse, D. Joubert, From ultrasoft pseudopotentials to the projector augmented-wave method, Phys. Rev. B. 59 (1999) 1758–1775, https://doi.org/10.1103/PhysRevB.59.1758.
[28] J.P. Perdew, K. Burke, M. Ernzerhof, Generalized gradient approximation made simple, Phys. Rev. Lett. 77 (1996) 3865–3868, https://doi.org/10.1103/PhysRevLett.77.3865.
[29] P. Haas, F. Tran, P. Blaha, Calculation of the lattice constant of solids with semilocal functionals, Phys. Rev. B Condens. Matter Mater. Phys. 79 (2009), 085104, https://doi.org/10.1103/PhysRevB.79.085104.
[30] S. Horoz, S. Simsek, S. Palaz, A.M. Mamedov, Electronic and optical properties of $KTaO_3$: ab initio calculation, World J. Condens. Matter Phys. 5 (2015) 78–85, https://doi.org/10.1016/j.physb.2007.02.012.
[31] G.H. Booth, T. Tsatsoulis, G.K.L. Chan, A. Grüneis, From plane waves to local Gaussians for the simulation of correlated periodic systems, J. Chem. Phys. 145 (2016), 084111, https://doi.org/10.1063/1.4961301.
[32] H. Jamnezhad, M. Jafari, Structural, electronic, and optical properties of C-type Gd_2O_3: a density functional theory investigation, J. Comput. Electron. 16 (2017) 272–279, https://doi.org/10.1007/s10825-017-0974-y.
[33] P. Larson, W.R.L. Lambrecht, A. Chantis, M. Van Schilfgaarde, Electronic structure of rare-earth nitrides using the LSDA+U approach: importance of allowing 4f orbitals to break the cubic crystal symmetry, Phys. Rev. B Condens. Matter Mater. Phys. 75 (2007) 1–14, https://doi.org/10.1103/PhysRevB.75.045114.
[34] S.L. Dudarev, G.A. Botton, S.Y. Savrasov, C.J. Humphreys, A.P. Sutton, Electron-energy-loss spectra and the structural stability of nickel oxide: an LSDA+U study, Phys. Rev. B. 57 (1998) 1505–1509.
[35] C.T. Koch, Determination of Core Structure Periodicity and Point Defect Density along Dislocations, Arizona State University, 2002.
[36] https://www.physics.hu-berlin.de/en/sem/software/software_qstem.
[37] B.D. Forbes, A.J. D'Alfonso, S.D. Findlay, D. Van Dyck, J.M. LeBeau, S. Stemmer, L.J. Allen, Thermal diffuse scattering in transmission electron microscopy, Ultramicroscopy 111 (2011) 1670–1680, https://doi.org/10.1016/j.ultramic.2011.09.017.
[38] M.J. Hÿtch, E. Snoeck, R. Kilaas, Quantitative measurement of displacement and strain fields from HREM micrographs, Ultramicroscopy 74 (1998) 131–146, https://doi.org/10.1016/S0304-3991(98)00035-7.
[39] P. Rajak, C.T. Koch, S. Bhattacharyya, Removal of supporting amorphous carbon film induced artefact from measured strain variation within a nanoparticle, Ultramicroscopy 199 (2019) 70–80, https://doi.org/10.1016/j.ultramic.2019.02.012.
[40] J.M. Cowley, High-resolution dark-field electron microscopy. I. Useful approximations, Acta Crystallogr. A 29 (1973) 529–536, https://doi.org/10.1107/s0567739473001324.
[41] R.F. Egerton, Electron Energy-Loss Spectroscopy in the Electron Microscope, second ed., Plenum Press, New York, 1996.
[42] P. Geuens, D. Van Dyck, The S-state model: a work horse for HRTEM, Ultramicroscopy 93 (2002) 179–198, https://doi.org/10.1016/S0304-3991(02)00276-0.
[43] A. Wang, F.R. Chen, S. Van Aert, D. Van Dyck, Direct structure inversion from exit waves. Part I: theory and simulations, Ultramicroscopy 110 (2010) 527–534, https://doi.org/10.1016/j.ultramic.2012.03.011.
[44] A. Wang, F.R. Chen, S. Van Aert, D. Van Dyck, Direct structure inversion from exit waves. Part II: a practical example, Ultramicroscopy 116 (2012) 77–85, https://doi.org/10.1016/j.ultramic.2012.03.011.
[45] F.R. Chen, D. Van Dyck, C. Kisielowski, In-line three-dimensional holography of nanocrystalline objects at atomic resolution, Nat. Commun. 7 (2016) 1–11, https://doi.org/10.1038/ncomms10603.